JACS
JOURNAL OF THE AMERICAN CHEMICAL SOCIETY

Article

pubs.acs.org/JACS

Light-Induced Conversion of Chemical Permeability to Enhance Electron and Molecular Transfer in Nanoscale Assemblies

Renata Balgley,[†] Graham de Ruiter,[†] Guennadi Evmenenko,[‡] Tatyana Bendikov,[§] Michal Lahav,*[,†] and Milko E. van der Boom*[,†]

[†]Department of Organic Chemistry, The Weizmann Institute of Science, 7610001 Rehovot, Israel

[‡]Department of Materials Science and Engineering, Northwestern University, Evanston, Illinois 60208, United States

[§]Department of Chemical Research Support, The Weizmann Institute of Science, Rehovot 7610001, Israel

Supporting Information

ABSTRACT: In this paper, we demonstrate how photochemically enhancing the permeability of metal−organic assemblies results in a significant enhancement of the electrochemical activity of metal complexes located within the assembly. The molecular assemblies consist of different layers of redox-active metal complexes ($[M(mbpy\text{-}py)_3][PF_6]_2$; M = Ru or Os) that are separated by redox-inactive spacers consisting of 1,4-bis[2-(4-pyridyl)ethenyl]benzene (**BPEB**) and $PdCl_2$ of variable thicknesses (0−13.4 nm). UV-irradiation (λ = 254 nm) of our assemblies induces a photochemical reaction in the redox-inactive spacer increasing the permeability of the assembly. The observed increase was evident by trapping organic ($^nBu_4NBF_4$) and inorganic ($NiCl_2$) salts inside the assemblies, and by evaluating the electrochemical response of quinones absorbed inside the molecular assemblies before and after UV irradiation. The increase in permeability is reflected by higher currents and a change in the directionality of electron transfer, i.e., from mono- to bidirectional, between the redox-active metal complexes and the electrode surface. The supramolecular structure of the assemblies dominates the overall electron transfer properties and overrules possible electron transfer mediated by the extensive π-conjugation of its individual organic components.

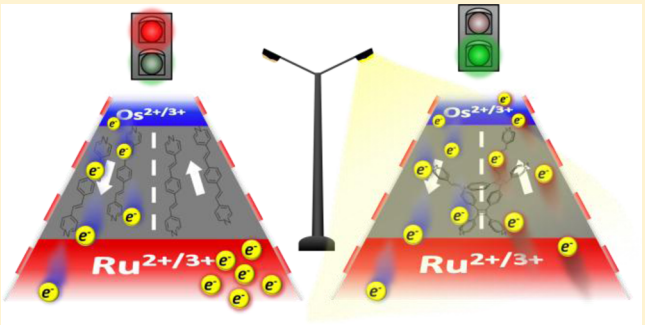

INTRODUCTION

Electron transfer (ET) through organic thin films has intrigued scientists for many years owing to their potential use.[1] Numerous studies have focused on ET across highly ordered self-assembled monolayers in which the conductivity increases as a function of π-conjugation or chain length of the molecular components.[2] Introducing relatively small modifications at the molecular level has significant consequences for ET properties in thin films.[2a−c,3] Factors that govern ET processes include (i) distance between the electron donor and acceptor, (ii) physical properties of the substrate (e.g., conducting vs semiconducting), (iii) degree of π-conjugation, and (iv) the medium in which the ET occurs, including the pH.[4] Defects and pinholes also play a key role.[2d]

The ET properties of metal complexes and assemblies thereof have also been studied[4f,5] with the prospect of applying such materials in data storage devices, solar cells, and smart windows.[6] Coordination chemistry plays an important role in constructing molecular wires and assemblies.[4a,5b−d,6a,c,e] Metal−organic assemblies have been reported with ultralow attenuation factors (β), and new models have been developed to realize these findings.[7] Several research groups have reported on the long-range ET properties of metal−organic wires. Rampi and Nishihara have used bis(terpyridine)-based ligands with different redox-active metal ions (Fe and Co) for the formation of rigid and highly conductive molecular wires,[3a,4a,7a,e] whereas Morris et al. have demonstrated a redox hopping charge transfer mechanism in electrocatalytic metallo-porphyrin-based metal−organic frameworks (MOFs).[7c] In a different study, Haga et al. recently investigated the thickness dependence of the charge migration rate in redox-active multilayers and developed the "stepping-stone mechanism" for long-range ET.[7d]

The advantage of using coordination-based metal−organic coatings is the organized manner in which these supramolecular structures can be arranged, while simultaneously allowing precise control over the assembly sequence and the amount of deposited material. These supramolecular structures are readily constructed by a sequence dependent layer-by-layer assembly technique in combination with the appropriate choice of ligand (number and type of binding sites and geometry) and metal ion. ET processes in such coatings have been studied mainly as a function of the molecular structure and sequence of the

Received: September 18, 2016
Published: November 14, 2016

DOI: 10.1021/jacs.6b09781
J. Am. Chem. Soc. 2016, 138, 16398−16406

Scheme 1. Schematic Representation of the Formation, Structure, and Electron Transfer Routes of Metal–Organic Assemblies [Ru-BPEB$_n$-Os] (n = 0–20)[a]

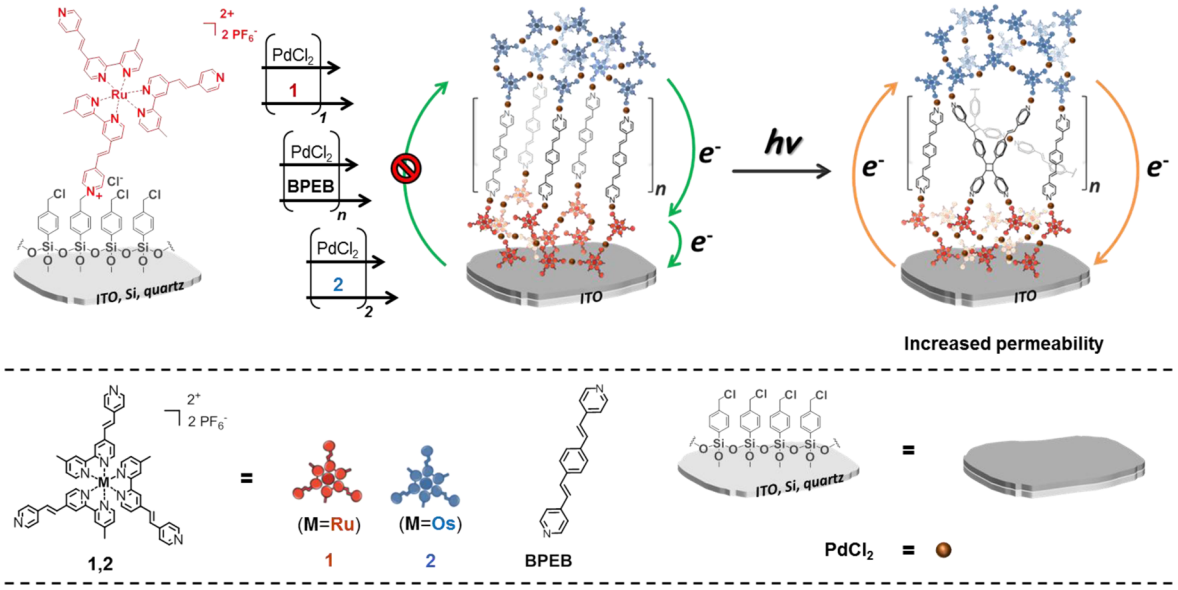

[a]The "sandwich-type" composition results from the sequence-dependent assembly and includes alternating deposition of one of the molecular components (**1**, **2**, or **BPEB**) and $PdCl_2(PhCN)_2$ from solution. The first layer is covalently attached to the surface.[8b] The photochemical reaction of **BPEB** is initiated by irradiating the assemblies with a Hg lamp (254 nm, 115 V, 60 Hz, 0.20 A) at a distance of 1 cm from the light source for 40 min. The result of the proposed photoreaction is illustrated on the right; the formation of other products cannot be excluded. For assemblies with thicknesses between 6.2 and 7.4 nm (n = 10–12; Figure 2C and G), the electron-transfer (ET) routes between the top layer (**2**) and the ITO electrode before and after UV irradiation are highlighted by the green and orange arrows. Before UV irradiation: The ET from the top layer (**2**) to the ITO electrode is mediated by the bottom layer (**1**), and the ET in the reversed direction is restricted due to the dense **BPEB** layer. After UV irradiation: direct ET between the top layer (**2**) and the ITO electrode is restored by increasing the permeability of the **BPEB** layer. For a detailed discussion of ET routes for n = 0–20, see Figure 2.

building blocks. We and others recently used sequence-dependent assembly to generate materials having different redox potentials at well-defined positions in the z-direction.[8] Precise control over the ET properties was achieved by depositing redox-active layers at defined positions inside the assembly.[8b] Despite numerous studies, controlling electrochemical communication and the directionality of ET between various elements inside thin films remains challenging.

Here we show how a noninvasive post-assembly modification changes the ET properties between redox-active polypyridyl complexes and the surface. Irradiating the assemblies with UV light (λ = 254 nm) induces a photochemical change in the redox-inactive spacer, enhancing the permeability of charge carriers inside these metal–organic films. The photochemical reaction significantly enhances the electrochemical communication between separate layers of redox-active polypyridyl complexes and controls the directionality of ET at the molecular level. Moreover, our method controls the permeability of the assemblies without significantly affecting their thickness, roughness, and composition. Other parameters that play a vital role in the ET and molecular-transfer properties were investigated as well.

RESULTS AND DISCUSSION

Ruthenium (**1**) and osmium (**2**) polypyridyl complexes, 1,4-bis[2-(4-pyridyl)ethenyl]benzene (**BPEB**), and $PdCl_2$ were utilized as building blocks for our metal–organic assemblies (Scheme 1). The pyridine groups of complexes **1**, **2**, and **BPEB**, combined with palladium(II)-coordination chemistry, enable the formation of well-ordered multicomponent assemblies. Redox-active complexes **1** and **2** were chosen for their well-separated oxidation potentials ($\Delta E_{1/2}$ > 0.40 V) and their relative stability under UV irradiation, whereas the photoactive chromophore (**BPEB**)—as well as $PdCl_2$—exhibits high stability in the potential window between 0.4 and 1.6 V. The use of **BPEB** also allowed us to fine-tune the distance between redox-active layers consisting of complexes **1** and **2** on a subnanometer scale and contributed to the high diversity of our material properties.

Metal–organic assemblies on silicon, quartz, and indium–tin oxide (ITO)-coated glass were formed by a sequence dependent assembly technique consisting of three distinct phases. In the first phase, silanized substrates—covalently modified with ruthenium complex **1**[8b]—were immersed in a solution of $PdCl_2(PhCN)_2$, followed by immersion into a solution of the ruthenium complex **1**. This process establishes the first redox-active layer with an oxidation potential of $E_{1/2}$ = 1.20 V (vs Ag/Ag^+). In the second phase of the self-assembly, the substrates are repetitively immersed into solutions of $PdCl_2(PhCN)_2$ and **BPEB**. During this phase the thickness of the **BPEB** domain is controlled at the subnanometer regime, where the **BPEP** thickness increases on average by ~0.7 nm per deposition cycle, while the length of the **BPEB** chromophore is ~1.6 nm. This increase is consistent with a slanted growth relative to the surface normal, as reported previously by our group.[8e] In the third and final phase of our assembly strategy the substrates are immersed in a solution of $PdCl_2(PhCN)_2$, followed by immersion in a solution of the osmium complex **2**. This establishes the second redox-active layer with an oxidation potential of $E_{1/2}$ = 0.77 V (vs Ag/Ag^+). The assemblies are

DOI: 10.1021/jacs.6b09781
J. Am. Chem. Soc. 2016, 138, 16398–16406

termed **Ru-BPEB$_n$-Os**, where **BPEB$_n$** signifies the amount of **BPEB** deposition steps (n = 0–20). Our procedure results in sandwich-type structures in which the metal complexes (**1**, **2**) are placed at predetermined positions within the metal–organic assemblies.

The assembly progress was followed by UV/vis spectroscopy. The three pyridine-based building blocks exhibit characteristic optical signatures in the UV and visible region (**1**, **2**, and **BPEB**; Figure 1). Each deposition cycle of $PdCl_2(PhCN)_2$ and

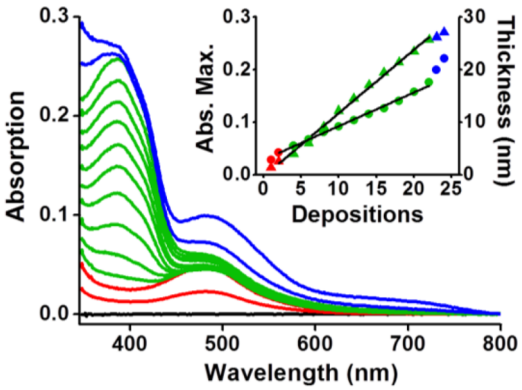

Figure 1. Optical absorption spectra of **Ru-BPEB$_{20}$-Os** on quartz substrates. The red traces represent the absorption spectra of the surface-confined ruthenium complexes **1**. The green traces represent the absorption spectra of **Ru-BPEB$_n$** assemblies (n = 2–20; only even deposition cycles are shown). The blue traces represent the absorption spectra of [**Ru-BPEB$_{20}$-Os**]. The inset shows the UV/vis absorption intensity (λ = 387 nm, ▲; left y-axis) and ellipsometry-derived thickness (●; right y-axis) vs the number of depositions steps. The red and the blue symbols represent layers consisting of complexes **1** and **2**, respectively. The second deposition of complex **1** is taken as the 0th point for the linear fit of the **BPEB**/$PdCl_2$ layer (all fits; R^2 > 0.99). The ellipsometry-derived thickness was obtained from assemblies grown on silicon substrates.

complex **1** or **2** is characterized by an increase in absorption of the singlet metal-to-ligand charge-transfer (^{1}MLCT) band at $\lambda \approx$ 500 nm. The deposition of the [**BPEB**]$_n$ spacer is characterized by the linear increase of the absorption band at λ = 387 nm (π to π^*) with respect to the number of deposition cycles (Figure 1, inset left y-axis). The linear increase is indicative of depositing a similar amount of chromophore density during each deposition step. Such regular solution-based depositions were corroborated by spectroscopic ellipsometry measurements that revealed a linear increase in the thickness of [**BPEB**]$_n$, in good agreement with the optical data (Figure 1, inset right y-axis).

The structural dependence of the ET properties was demonstrated by photochemically altering the molecular structure of the spacer [**BPEB**]$_n$ and addressing the length (n = 0–20; 0–13.4 nm). Conjugated molecules such as **BPEB** are known to undergo [2 + 2] photocycloaddition reactions in the solid state, in crystals, or as monolayers bound to solid surfaces.[9] Such post-assembly modifications could have a pronounced effect on the optical and electrochemical properties of our composites. We found that irradiating **Ru-BPEB$_n$-Os** at λ = 254 nm and at an optimal time of 40 min resulted in significant bleaching of the **BPEB** band at $\lambda \approx$ 387 nm, with only a minor change in the ^{1}MLCT band associated with complexes **1** and **2** (Figures 2A–D, S1A, and Table S1). Prolonged reaction times result in a decrease of the intensity of the ^{1}MLCT band at $\lambda \approx$ 500 nm (Figures S1A–C). The reduced absorption band at $\lambda \approx$ 387 nm is characteristic for reduction in conjugation of **BPEB**.[9a] Further structural evidence is provided by attenuated total reflection Fourier transform infrared (ATR-FTIR) spectroscopy of **Ru-BPEB$_{20}$-Os** on silicon substrates (Figure S2). We observed a notable decrease (~38%) in the intensity of the band at ν = 1612 cm^{-1}, which corresponds to the stretching of *trans*-disubstituted double bonds.[10] The residual intensity of this band indicates that some double bonds are still present. The optical data also indicate that not all **BPEB** molecules have reacted (Figure 2B–D), consistent with the IR data. Since intermolecular photochemical reactions require precise positioning and orientation of the reacting molecules, the reaction yield is not expected to be quantitative. Although the spectroscopic data are consistent with a [2 + 2] photocycloaddition,[9] the formation of other products cannot be excluded.

A series of cyclic voltammetry (CV) experiments were performed in order to investigate the effect of photoirradiation on the ET properties of the assemblies (Figure 2E–H). By systematically increasing the distance between the **1**- and **2**-based redox-active layers, insight was obtained between the interplay of spacer length and photoirradiation and their combined effect on ET pathways. Depending on the **BPEP** thickness, three distinct electrochemical regimes can be recognized:

(a) [**BPEB**]$_n$ (n = 0–4) < 2.5 nm: The assemblies exhibit reversible electrochemical waves for both the $Os^{2+/3+}$ and $Ru^{2+/3+}$ redox couples at half-wave potentials similar to the corresponding complexes in solution ($E_{1/2}$ = 1.20 V (**1**), and 0.77 V (**2**)). A representative CV of **Ru-BPEB$_0$-Os**, having no **BPEB**/$PdCl_2$ and a total thickness of 8.7 nm, is shown in Figure 2E (green trace). The half-wave potentials of complexes **1** and **2** are 1.21 and 0.75 V (vs Ag/Ag^+), respectively. UV irradiation does not affect the electrochemistry of this assembly (Figure 2E, orange trace). The Ru and Os centers are similarly addressed by the ITO electrode before and after irradiation.

(b) [**BPEB**]$_n$ (n = 4–12) thickness between 2.5 and 7.4 nm: The current magnitude of the $Os^{2+/3+}$ redox couple decreases (anodic peak current: from 0.09 to 0.02 mA; cathodic peak current: from −0.09 to −0.02 mA), as seen in Figure 2F and G, green traces. At the same time, a catalytic oxidative prewave appears at E = 1.03–1.13 V (Figure 2F and G). This decrease in current and the appearance of the catalytic prewave are a direct result of the **BPEB** interfering with ET. At these distances communication between the Os-metal centers is hampered, resulting in a lower current intensity at $E_{1/2}$ ≈ 0.8 V. However, at the onset potential for Ru-oxidation (~1.1 V), the Ru-metal center can catalytically oxidize the Os metal centers, due to the shorter distance between **1** and **2** (2.4–7.4 nm), compared to **2** and the electrode surface (6.6–11.6 nm). Since oxidation is possible during anodic scans, this process results in unidirectional ET.[11] Interestingly, irradiating the assemblies with UV-light results in nearly complete restoration of the electrochemical reversibility of the $Os^{2+/3+}$ redox couple. Figure 2F and 2G (orange traces) reveal increased peak currents of the $Os^{2+/3+}$ redox couple, whereas the catalytic wave currents decrease significantly. We observed that the ET from the **2**-based layer to the

DOI: 10.1021/jacs.6b09781
J. Am. Chem. Soc. 2016, 138, 16398–16406

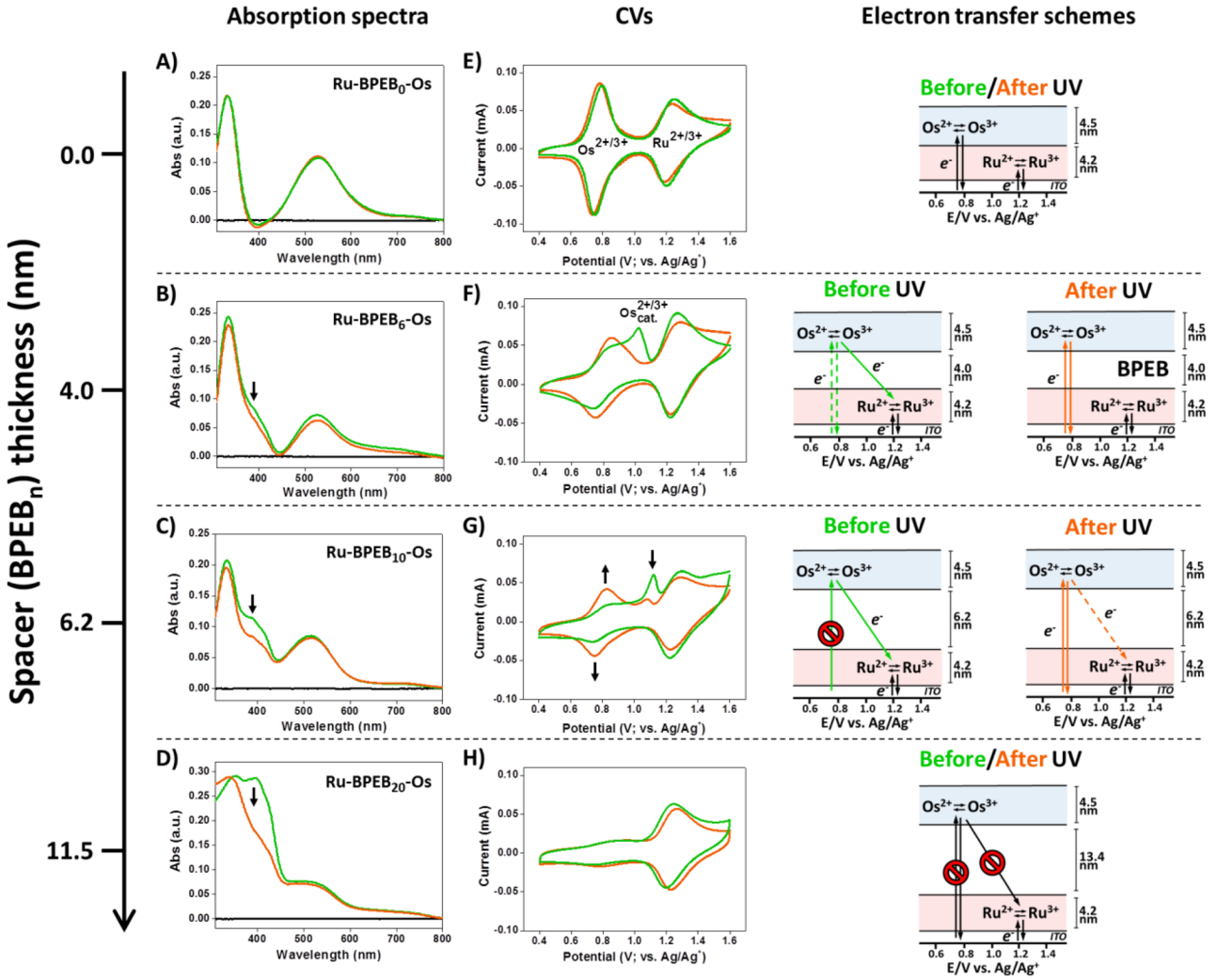

Figure 2. UV/vis spectra (A–D) and cyclic voltammograms (CVs; E–H) of **Ru-BPEB$_0$-Os** (A, E), **Ru-BPEB$_6$-Os** (B, F), **Ru-BPEB$_{10}$-Os** (C, G), and **Ru-BPEB$_{20}$-Os** (D, H) on ITO substrates, before (green trace) and after (orange trace) UV irradiation. UV irradiation was performed under the same conditions as mentioned in Scheme 1. CVs were recorded in 0.1 M $TBAPF_6/CH_3CN$, at a scan rate of 100 mV s^{-1}, using ITO, Pt, and Ag wires as working, counter, and reference electrodes, respectively. The arrows emphasize the change in the absorption (B–D) and the peak currents (G) following UV irradiation. The corresponding electron transfer (ET) schemes before and after UV irradiation are shown on the right.

underlying electrode is substantially facilitated following the photoreaction, despite the partial loss of C=C bond character in **BPEB**.

(c) [**BPEB**]$_n$ (n > 12) > 7.4 nm: At these distances—irrespective of UV irradiation—almost complete electrochemical isolation of the Os centers occurs, and the current associated with the $Os^{2+/3+}$ redox couple has nearly disappeared. The small amount of remaining signal is most likely due to ET through defects and pinholes (Figure 2H).

In order to trace the origin of these remarkable ET properties, we compared the structural features of the assemblies before and after UV irradiation. The photochemical reactions result in a remarkable increase in the networks' permeability, as probed by two electroactive quinones; 2-*tert*-butylbenzoquinone (**Q1**) and 3,3′,5,5′-tetra-*tert*-butyldiphenoquinone (**Q2**).[12] CVs with **Q1** or **Q2** added to the supporting electrolyte were recorded with bare ITO and ITO electrodes functionalized with **Ru-BPEB$_6$-Os**, **Ru-BPEB$_{10}$-Os**, or **Ru-BPEB$_{20}$-Os**, before and after UV irradiation (Figures 3 and S3).

The increased electrochemical activity of **Q1** (206 Å^3) and **Q2** (640 Å^3) after UV irradiation of the assemblies indicates higher network permeability (Figure 3A–C). This effect is more pronounced with the smaller **Q1** compared to the larger **Q2**. In addition, a significant reduction in the electrochemical activity of both quinones is observed with increasing spacer thickness. An assembly with a short spacer (n = 6) results in a more pronounced electrochemical response of **Q1**, since its pathway toward the electrode surface is shorter. **Ru-BPEB$_6$-Os** also exhibits the largest difference in the electrochemical accessibility of **Q1** before and after UV irradiation (Figure 3A). For **Ru-BPEB$_{20}$-Os**, the current is dramatically decreased, both before and after UV irradiation, because of efficient blocking of the ITO surface by the assembly, and due to the size (640 Å^3) of the quinone (Figure S3). The increase in current before UV irradiation of **Ru-BPEB$_6$-Os** compared to the bare ITO electrode (Figure 3A; green and dashed traces) is explained by trapping of the quinone inside the network, which hampers their diffusion back to the bulk.

Further permeability experiments were performed by trapping inorganic and organic salts inside **Ru-BPEB$_{10}$-Os**

DOI: 10.1021/jacs.6b09781
J. Am. Chem. Soc. 2016, 138, 16398–16406

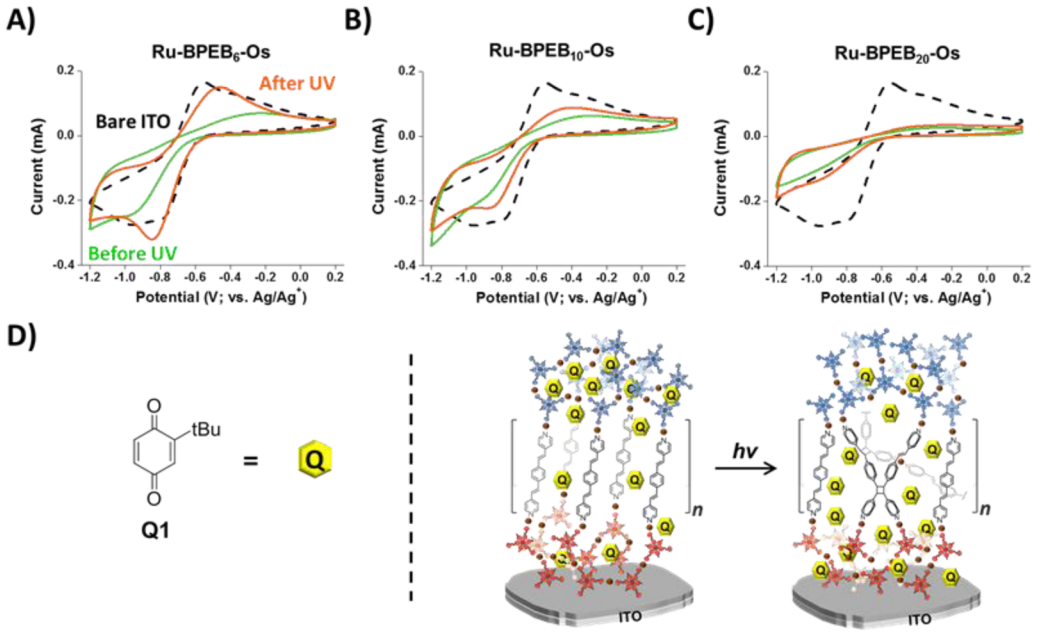

Figure 3. Cyclic voltammograms (CVs) of 1.0 mM solutions of 2-*tert*-butylbenzoquinone (**Q1**) with **Ru-BPEB$_6$-Os** (A), **Ru-BPEB$_{10}$-Os** (B), and **Ru-BPEB$_{20}$-Os** (C), grown on ITO, before (green trace) and after (orange trace) UV irradiation. The dashed traces represent the CVs of **Q1** with bare ITO as the working electrode. The CVs were recorded at room temperature in dry 0.05 M $TBAPF_6/CH_3CN$ under an inert atmosphere at a scan rate of 100 mV s^{-1}. Pt and Ag wires were used as counter and reference electrodes, respectively. UV irradiation was carried out under the same conditions as those in Scheme 1. (D) Molecular structure of **Q1** and a schematic representation of the coordination-based assemblies before and after UV irradiation. Formation of other products cannot be excluded. n = 6 (A), 10 (B), or 20 (C). For CVs of 3,3′,5,5′-*tetra-tert*-butyldiphenoquinone (**Q2**), see Figure S3.

before and after UV irradiation. The ITO-bound assemblies were immersed for 30 min in the following solutions: (a) $NiCl_2·6H_2O$ in ethanol (10 mM), (b) tetrabutylammonium tetrafluoroborate (^{n}Bu$_4$NBF$_4$) in acetonitrile (0.1 M), and (c) tetrabutylammonium tetraphenylborate (^{n}Bu$_4$NBPh$_4$) in acetonitrile (0.1 M). The substrates were washed with ethanol (a) or acetonitrile (b and c) and subsequently dried. The elemental composition of the films, including the trapped salts, were analyzed by X-ray photoelectron spectroscopy (XPS; Table 1 and Figure 4). Based on the formation of a fully formed coordination network, the expected elemental ratios are estimated to be N/Pd = 4, Os/Ru = 1, and N/(Os + Ru) = 14. The observed experimental ratios before and after irradiation are in very good agreement with the calculated expected values (Table 1).

Table 1. XPS-Derived Elemental Ratios of Ru-BPEB$_{10}$-Os before and after UV Irradiation,[a] after Immersion in $NiCl_2$ or ^{n}Bu$_4$NBF$_4$ Solutions[b]

	Before UV	After UV	After UV/Before UV
		$NiCl_2$	
Os/Ru	1.1	1.4	1.3
N/Pd	3.6	4.0	1.1
N/(Os+Ru)	16.8	16.6	1.0
Ni/Pd	0.6	2.5	4.2
		^{n}Bu$_4$NBF$_4$	
N^+/N	0.1	0.2	2.0
N^+/B	0.9	1.1	1.2

[a]According to the conditions described in Scheme 1. [b]See experimental details and Figure 4.

The data also show that after UV irradiation a marked increase (4×) is observed in the nickel content, indicating the increased storage of $NiCl_2$ inside the molecular assembly (Table 1, Figure 4A). The concentrations of other elements such as Pd—used as internal standard—are not affected (Figure 4A, inset). Likewise, for organic salts (^{n}Bu$_4$NBF$_4$) a similar effect was observed. After photoirradiation, an increase (2×) in the content of ^{n}Bu$_4$NBF$_4$ was observed (Table 1, Figure 4B). The near unity of the N^+/B ratio shows that the observed increase is due to incorporation of ^{n}Bu$_4$NBF$_4$ and not due to salt metathesis with the anion (PF_6^-) of the molecular assembly. Regardless of photoirradiation, no XPS signals were detected for ^{n}Bu$_4$NBPh$_4$ due to the large size of the anion (Figure 4C). These observations are in very good agreement with the results of the electrochemical experiments with the quinones and confirm the increase in permeability of the films upon photoirradiation.

Considering the observed change in permeability before and after UV irradiation, we hypothesize that the photochemical reaction facilitates the movement of charge carriers across the assembly. ET processes in surface-confined systems are strongly dependent on the diffusion of the supporting electrolyte for maintaining electroneutrality during redox reactions.[13] Upon increasing the $TBAPF_6$ concentration from 0.01 to 0.50 M, the peak currents increase for both the metal complexes **1** and **2** before and after UV irradiation of **Ru-BPEB$_6$-Os** (Figure S4 and Table S2). The effects of both the UV irradiation and the electrolyte concentration indicate that ET through the conjugated backbone of **BPEB** is of minor importance. This observation is expected and is in agreement with reported experimental and theoretical studies that rule out a significant conjugation between the conjugated popypyridyl-based components, coordinated through $PdCl_2$.[14] The differences in the

DOI: 10.1021/jacs.6b09781
J. Am. Chem. Soc. 2016, 138, 16398−16406

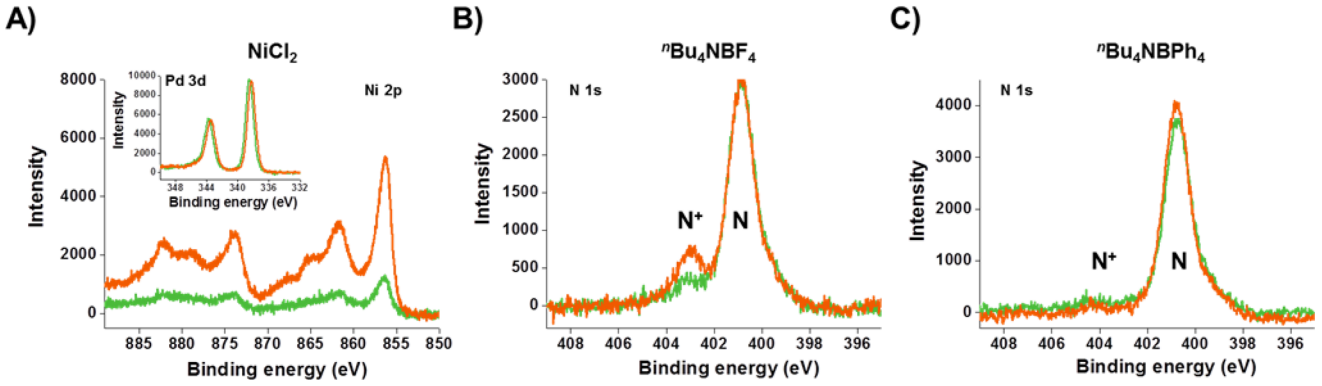

Figure 4. X-ray photoelectron spectroscopy (XPS) signals of **Ru-BPEB$_{10}$-Os** on an ITO substrate before (green trace) and after (orange trace) UV irradiation, according to the conditions described in Scheme 1. The substrates were immersed in solutions of $NiCl_2$ (A), $^nBu_4NBF_4$ (B), and $^nBu_4NBPh_4$ (C).

electrochemical properties of the assemblies before and after UV irradiation (as shown in Figure 2) are not because of variations of their composition, thickness, and roughness, as confirmed by spectroscopic ellipsometry, atomic force microscopy (AFM), synchrotron X-ray reflectivity (XRR), and X-ray photoelectron spectroscopy (XPS).

The spectroscopic ellipsometry-derived thickness of five different assemblies ([**Ru-BPEB$_n$-Os**], n = 4, 8, 12, 18, and 20) was measured before and after UV irradiation. From the results summarized in Table 2 it is clear that the irradiation has no noticeable effect on the film thickness. This observation implies that the terminal **2**-based layer remains at the same distance from the substrate surface. Atomic force microscopy (AFM) images of **Ru-BPEB$_o$-Os**, **Ru-BPEB$_{10}$-Os**, and **Ru-BPEB$_{20}$-Os** before and after UV irradiation are presented in Figures 5 and S5. Increasing the thickness of [**BPEB**]$_n$ (from 0 to 13.4 nm; n = 0 → 20) results only in a minor increase in the surface root-mean-square roughness (R_q; from 0.3 to 0.7 nm). Upon UV irradiation no significant changes in both the morphology and root-mean-square roughness of the molecular assemblies are observed (Figure S5). For instance, for **Ru-BPEB$_{10}$-Os** only minor changes in the roughness values (R_q) are observed before (0.51 nm) and after (0.50 nm) UV irradiation (Figure 5).

To further investigate the composition of our molecular assemblies, XRR measurements were performed on **Ru-BPEB$_{10}$-Os** and **Ru-BPEB$_{14}$-Os** before and after UV irradiation (Figures 6A, S6). The thickness, surface roughness, and electron density (ED) profiles of the assemblies were obtained from the specular reflectivity spectra (Figure S6A and B).[16] The ED plots exhibit distinct fluctuations that correspond to the four regions (Figure 6A) of the samples: (i) Si/SiO_x (the substrate), (ii) **1**-based layer, (iii) [**BPEB**]$_n$, and (iv) **2**-based layer. Regions *ii* and *iv* exhibit higher EDs compared with region *iii*, which is in agreement with the presence of the Os and Ru metal centers which have a high electron density. The similarity in ED profiles before and after irradiation (Figure 6A green and orange trace) combined with the excellent agreement between the XRR and ellipsometric derived thickness and AFM derived roughness indicate that the composition of the assemblies remains virtually unchanged (Table S3).

Table 2. Ellipsometry-derived Thicknesses of the Assemblies before and after UV Irradiation[a]

Assembly	Thickness (nm)	
	Before UV	After UV
Ru-BPEB$_4$-Os	8.6	8.8
Ru-BPEB$_8$-Os	10.5	10.4
Ru-BPEB$_{12}$-Os	12.2	12.3
Ru-BPEB$_{18}$-Os	18.2	18.0
Ru-BPEB$_{20}$-Os	22.1	21.4

[a]Standard deviation <4%.

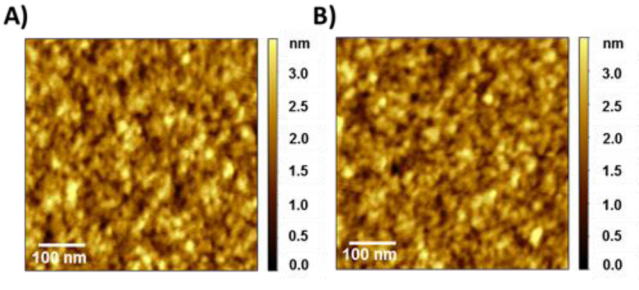

Figure 5. AFM topography images of **Ru-BPEB$_{10}$-Os** on silicon substrates before (A) and after (B) UV irradiation as described in Scheme 1. The scan area is 500 nm × 500 nm, and the root-mean-square roughness (R_q) values are 0.51 nm (A) and 0.50 nm (B).

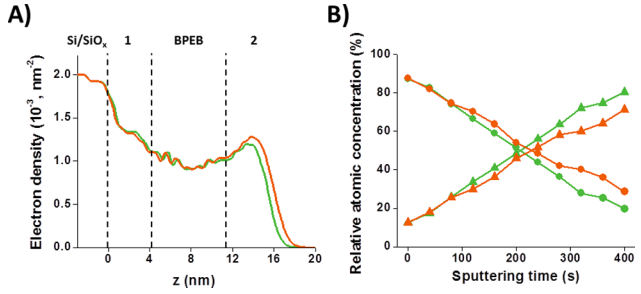

Figure 6. (A) Representative synchrotron X-ray reflectivity (XRR)-derived electron density profiles for **Ru-BPEB$_{14}$-Os** before (green; thickness, 15.4 nm; roughness, 0.9 nm) and after (orange; thickness, 16.0 nm; roughness, 1.0 nm) UV irradiation. Si/SiO_x substrate: −2.0−0 nm. **1**-based layer: 0−4.2 nm including the siloxane-based coupling layer. [**BPEB**]$_n$: 4.2−11.5 nm. **2**-based layers: 11.5−16.0 nm. (B) In-depth profiling by X-ray photoelectron spectroscopy (XPS). Relative atomic concentration of Os (●) and Ru (▲) vs sputtering time of **Ru-BPEB$_{20}$-Os** on ITO, before (green traces) and after (orange traces) UV irradiation. For more details, see Table 1.

DOI: 10.1021/jacs.6b09781
J. Am. Chem. Soc. 2016, 138, 16398−16406

In-depth profiling by XPS was performed on the **Ru-BPEB$_{20}$-Os** assembly on ITO, before and after UV irradiation, in order to determine the elemental composition. The samples were sputtered with large argon ion clusters for up to 400 s, while the relative atomic concentrations of Ru and Os in the remaining assembly were being measured. Figure S7 shows the major signals of Ru $3d_{5/2}$ and Os $4d_{5/2}$. Before sputtering, the intensity of the Os 4d band is high and that of Ru 3d is low. However, after 400 s of sputtering, about 20% of Os remains on the surface and the intensity of the Ru band increases significantly. The magnitude of the Ru and Os bands is comparable before and after UV irradiation during sputtering. As observed from the data presented in Figure 6B, the atomic concentration of Os continuously decreases under progressive sputtering, both before and after irradiation. Similarly, the signal of Ru grows as the thickness of the assembly decreases. The residual Os signal, after long sputtering times, is due to remnants of this heavy atom on the surface and to the high roughness of the ITO substrate. Owing to these factors, a continuous change in the atomic concentrations of Ru and Os was observed, rather than clear interfaces, as seen by XRR. Overall, we conclude that the vertical composition of the assemblies remains unchanged after UV irradiation.

CONCLUDING REMARKS

In conclusion, by using photoresponsive metal−organic oligomers, we could alter the molecular structure of our assemblies by UV light, while keeping the composition, thickness, and roughness constant. In-depth profiling of the assemblies before and after UV irradiation confirms that the relative positions of the redox-active components are not affected by the photochemical reaction. As expected, the conjugation of the interlayer spacers plays a relatively minor role in the ET properties;[14] rather, the distance between the redox-active layers and their permeability play a major role. Increasing the permeability results in a higher charge carrier density, which, in turn, results in increased electrochemical reversibility of the Os- and Ru-based redox processes. Hence, by using a noninvasive post-assembly modification, we can control the directionality and reversibility of ET. These results advance our understanding of electrochemical processes in metal−organic assemblies and the factors governing it (i.e., structural diversity of the assembly). We believe that our systems are of interest in the context of developing novel electrochromic films, memristors, rectifiers, and memory elements.[6d,17a,b,18]

EXPERIMENTAL SECTION

Materials. Complexes **1**−**2**, 1,4-bis[2-(4-pyridyl)-ethenyl]benzene (**BPEB**), and $PdCl_2(PhCN)_2$ were synthesized according to published procedures.[17a,b,d,e] *p*-Chloromethyl-phenyltrichlorosilane was purchased from Gelest, Inc. 2-*tert*-Butyl-1,4-benzoquinone (**Q1**) was purchased from Alfa Aesar. Tetrabutylammonium hexafluorophosphate ($TBAPF_6$), 3,3′,5,5′-tetra-*tert*-butyldiphenoquinone (**Q2**), and anhydrous CH_3CN (H_2O < 0.001% v/v) were purchased from Aldrich. Solvents (AR grade) were purchased from Bio-Lab (Jerusalem), Frutarom (Haifa), or Mallinckrodt Baker (Phillipsburg, NJ). Toluene was dried and purified using a M. Braun solvent purification system and degassed before introduction into an M. Braun glovebox. Single-crystal silicon ⟨100⟩ wafers were purchased from Wafernet (San Jose, CA) and Indium−Tin Oxide (ITO)-coated glass substrates (7.5 cm × 0.8 cm) were purchased from Delta Technologies (Loveland, CO). ITO and silicon substrates were cleaned by sonication in organic solvents. They were subsequently dried under a N_2 stream and cleaned for 30 min with a UVOCS cleaning system (Montgomery, PA). Quartz substrates (2.0 cm × 1.0 cm) were purchased from Chemglass, Inc. and were cleaned by immersion in a "piranha" solution (7:3 (v/v) H_2SO_4/30% H_2O_2) for 1 h. ***Caution:*** *piranha solution is an extremely dangerous oxidizing agent and should be handled with care using appropriate personal protection.* The substrates were then rinsed with DI water followed by the RCA cleaning protocol: 1:5:1 (v/v) NH_4OH/H_2O/30% H_2O_2 at 80 °C for 45 min. The substrates were washed several times with DI water and then with isopropanol and dried under a N_2 stream. All substrates were dried at 130 °C for 2 h. The siloxane-based chemistry and the formation of the **1**-based template layer were carried out in a glovebox or by using standard Schlenk-cannula techniques, as described elsewhere.[17a−c]

Physical Methods. UV/vis spectroscopy was carried out using a Cary 100 spectrophotometer. Thicknesses were estimated by spectroscopic ellipsometry on an M-2000 V variable angle instrument (J. A. Woollam Co., Inc.) with VASE32 software. Electrochemical measurements (i.e., cyclic voltammetry) were performed using a potentiostat (CHI660A) in a three-electrode cell configuration consisting of the functionalized ITO substrate, Pt wire, and Ag wire as working, counter, and reference electrodes, respectively. Solutions of $TBAPF_6$ in CH_3CN (0.1 M, unless stated otherwise) were used as the supporting electrolyte. Attenuated total reflectance Fourier-transform infrared (ATR-FTIR) spectroscopic measurements were performed using a Bruker Equinox-55 spectrometer with a liquid N_2 cooled mercury cadmium telluride (MCT) detector. Spectra were averaged over 128 scans and referenced to a freshly cleaned silicon substrate. Atomic force microscopy (AFM) images were recorded using an NT-MDT NTEGRA with an SU005 head and a 100 μm bottom scanner. APPNano Access-FM probe was used in semicontact mode. All experiments were carried out at room temperature. For sample depth profiling, a Kratos Argon Gas Cluster Ion Source (GCIS) integrated into a Kratos AXIS Nova system was applied in a mode selecting Ar_{2000}+ clusters, accelerated to 5 kV, such that a partition energy of 2.5 eV per atom is obtained. The large raster size (3.5 × 3.5 mm^2) was chosen for two reasons: (1) to keep the etch rate as low as possible; (2) to ensure that recorded data is within the crater. XPS measurements were carried out using a monochromatic Al Kα X-ray source ($h\nu$ = 1486.6 eV) at 600 W and detection pass energies ranging between 20 and 160 eV. A low-energy electron flood gun (eFG) was applied for charge neutralization. Curve fitting analysis was based on linear, Shirley or Tougaard background subtraction and application of Gaussian−Lorenzian line shapes. Relative atomic concentrations were calculated based on the Ru 3d and Os 4d signals (in counts per second, or CPS units), taking into account the individual sensitivity factor (S.F). XRR data were collected at the 12-BM-B beamline at the Advanced Photon Source (APS) in the Argonne National Laboratory (Argonne, IL), using a Huber four-circle diffractometer in the specular reflection mode (*i.e.*, the incident angle is equal to the exit angle θ). X-rays of energy E = 10 keV (λ = 1.24 Å) were used for these measurements. The beam size was 0.40 mm vertically and 0.60 mm horizontally. The samples were placed under helium during measurements to reduce background scattering and radiation damage. Finally, the XRR data were analyzed using Parratt's model-independent fitting formalism.[17f] Braun, C. Parratt32 Software for Reflectivity; HMI: Berlin, 1999.

The dimensions of the quinones were derived from calculations using Gaussian09 Revision E.01.[19a] Geometries were optimized with the Perdew−Burke−Ernzerhof (PBE)[19b,c] density functional using the def2-SVP (double-ζ plus polarization quality) basis set[19d,e] and the Weigend-06 (W06)[19e,f] density fitting basis set.[19g,h]

Formation of Ru-BPEB$_n$-Os. Substrates functionalized with a **1**-based template layer (Scheme 1)[17a,b] were loaded onto a Teflon holder and immersed for 15 min in a 1.0 mM solution of $PdCl_2(PhCN)_2$ in THF. The samples were then sonicated in THF and in acetone for 3 min each. Subsequently, the samples were immersed in a 0.2 mM solution of compound **1** in THF/DMF (9:1, v/v) for 15 min. The samples were then sonicated in THF and in acetone for 5 min each (= first deposition cycle). Next, the samples were immersed for 10 min in a 1.0 mM solution of $PdCl_2(PhCN)_2$ in

DOI: 10.1021/jacs.6b09781
J. Am. Chem. Soc. 2016, 138, 16398−16406

THF and then sonicated in THF and in acetone for 3 min each. Thereafter, the samples were immersed for 10 min in a 1.0 mM solution of **BPEB** in THF and sonicated in THF and in acetone for 3 min each (= second deposition cycle). The second deposition cycle procedure was repeated for 0 to 20 deposition cycles of **BPEB** (only slides with an even number of **BPEB** deposition cycles were kept for subsequent depositions of complex **2**). Then, the first deposition cycle procedure was repeated (2 ×) using a 0.2 mM solution of complex **2** in THF/DMF (9:1, v/v). Finally, the samples were rinsed in ethanol and dried under a stream of N_2. All steps were carried out at room temperature. Three separate $PdCl_2(PhCN)_2$ solutions with identical concentrations were used to rigorously exclude possible cross contaminations between compounds **1**, **2**, and **BPEB**.

Irradiation Conditions. The samples were placed at a distance of 1 cm from a Hg lamp (254 nm, 115 V, 60 Hz, 0.20 A) and were irradiated for 40 min, unless stated otherwise.

Quinone Electrochemical Experiments. CVs of 0.1 M solutions of 2-*tert*-butyl-1,4-benzoquinone (**Q1**) and 3,3′,5,5′-tetra-*tert*-butyldiphenoquinone (**Q2**) were recorded using a bare ITO and an ITO functionalized with the molecular assemblies as the working electrode, Pt wire as a counter electrode, and Ag wire as the reference electrode. TBAPF6 (0.05 M) in dry acetonitrile was used as the supporting electrolyte solution. The measurements were performed under an inert atmosphere at room temperature.

Trapping Experiments. ITO substrates functionalized with **Ru-BPEB$_{10}$-Os** before and after UV irradiation were immersed in (a) 10 mM ethanol solution of $NiCl_2{\cdot}6H_2O$, (b) 0.1 M acetonitrile solution of *tetra*-butylammonium tetrafluoroborate ($^nBu_4NBF_4$), and (c) 0.1 M acetonitrile solution of *tetra*-butylammonium tetraphenylborate ($^nBu_4NBPh_4$). The substrates were immersed for 30 min, after which they were washed in ethanol (a) or acetonitrile (b and c) solutions and dried. The experiments were performed at room temperature.

Electrolyte Concentration Dependence. CVs of **Ru-BPEB$_6$-Os** on ITO were recorded using Pt and Ag wires as counter and reference electrodes, respectively. Acetonitrile solutions of the following concentrations of $TBAPF_6$ were used as the supporting electrolyte: 0.01, 0.10, and 0.50 M. The measurements were performed in air at room temperature.

■ ASSOCIATED CONTENT

Supporting Information

The Supporting Information is available free of charge on the ACS Publications website at DOI: 10.1021/jacs.6b09781.

Figures S1−S7 and Tables S1−S3 (PDF)

■ AUTHOR INFORMATION

Corresponding Authors

*michal.lahav@weizmann.ac.il

*milko.vanderboom@weizmann.ac.il

ORCID

Milko E. van der Boom: 0000-0003-4102-4220

Notes

The authors declare no competing financial interest.

■ ACKNOWLEDGMENTS

This research was supported by the Ministry of Science, Technology & Space, Israel, the Helen and Martin Kimmel Center for Molecular Design, Mary and Tom Beck-Canadian Center for Alternative Energy Research, David Rosenberg (Chicago, IL), the Yeda-Sela Center for Basic Research, a research grant from the Leona M. and Harry B. Helmsley Charitable Trust, the Israel Science Foundation (ISF) Grant No. 1023/13. G.E. gratefully acknowledges support from the Center for Electrochemical Energy Science, an Energy Frontier Research Center funded by the U.S. Department of Energy, Office of Science, Office of Basic Energy Sciences, under Contract No. DE-AC02-06CH11357. M.E.vdB. is the incumbent of the Bruce A. Pearlman Professional Chair in Synthetic Organic Chemistry. We thank Dr. Simon Hutton (Kratos Analytical Ltd) for carrying out the XPS experiments, Dr. Mark. A. Iron for carrying out molecular volume calculations, and Dr. Sidney Cohen for carrying out the AFM measurements.

■ REFERENCES

(1) (a) Taherinia, D.; Smith, C. E.; Ghosh, S.; Odoh, S. O.; Balhorn, L.; Gagliardi, L.; Cramer, C. J.; Frisbie, C. D. *ACS Nano* **2016**, *10*, 4372. (b) Yuan, L.; Breuer, R.; Jiang, L.; Schmittel, M.; Nijhuis, C. A. *Nano Lett.* **2015**, *15*, 5506. (c) Xing, G.; Mathews, N.; Sun, S.; Lim, S. S.; Lam, Y. M.; Grätzel, M.; Mhaisalkar, S.; Sum, T. C. *Science* **2013**, *342*, 344. (d) Cahen, D.; Hodes, G. *Adv. Mater.* **2002**, *14*, 789.

(2) (a) Salomon, A.; Cahen, D.; Lindsay, S.; Tomfohr, J.; Engelkes, V. B.; Frisbie, C. D. *Adv. Mater.* **2003**, *15*, 1881. (b) Wold, D. J.; Haag, R.; Rampi, M. A.; Frisbie, C. D. *J. Phys. Chem. B* **2002**, *106*, 2813. (c) Holmlin, R. E.; Haag, R.; Chabinyc, M. L.; Ismagilov, R. F.; Cohen, A. E.; Terfort, A.; Rampi, M. A.; Whitesides, G. M. *J. Am. Chem. Soc.* **2001**, *123*, 5075. (d) Love, J. C.; Estroff, L. A.; Kriebel, J. K.; Nuzzo, R. G.; Whitesides, G. M. *Chem. Rev.* **2005**, *105*, 1103.

(3) (a) Maeda, H.; Sakamoto, R.; Nishihara, H. *J. Electroanal. Chem.* **2016**, *779*, 112. (b) Zhao, Y.; Zhao, X.; Zang, Y.; Di, C.; Diao, Y.; Mei, J. *Macromolecules* **2015**, *48*, 2048.

(4) (a) Sakamoto, R.; Katagiri, S.; Maeda, H.; Nishimori, Y.; Miyashita, S.; Nishihara, H. *J. Am. Chem. Soc.* **2015**, *137*, 734. (b) Noriega, R.; Rivnay, J.; Vandewal, K.; Koch, F. P. V; Stingelin, N.; Smith, P.; Toney, M. F.; Salleo, A. *Nat. Mater.* **2013**, *12*, 1038. (c) Wenger, O. S. *Acc. Chem. Res.* **2011**, *44*, 25. (d) Zhu, J.; Shim, B. S.; Di Prima, M.; Kotov, N. A. *J. Am. Chem. Soc.* **2011**, *133*, 7450. (e) DiBenedetto, S. A.; Facchetti, A.; Ratner, M. A.; Marks, T. J. *J. Am. Chem. Soc.* **2009**, *131*, 7158. (f) Cornil, J.; Beljonne, D.; Calbert, J.-P.; Brédas, J.-L. *Adv. Mater.* **2001**, *13*, 1053.

(5) (a) Meng, F.; Hervault, Y.-M.; Shao, Q.; Hu, B.; Norel, L.; Rigaut, S.; Chen, X. *Nat. Commun.* **2014**, *5*, 3023. (b) Kumar, A.; Chhatwal, M.; Mondal, P. C.; Singh, V.; Singh, A. K.; Cristaldi, D. A.; Gupta, R. D.; Gulino, A. *Chem. Commun.* **2014**, *50*, 3783. (c) Forster, R. J.; Keyes, T. E. *Coord. Chem. Rev.* **2009**, *253*, 1833. (d) Concepcion, J. J.; Jurss, J. W.; Brennaman, M. K.; Hoertz, P. G.; Patrocinio, A. O. T.; Murakami Iha, N. Y.; Templeton, J. L.; Meyer, T. J. *Acc. Chem. Res.* **2009**, *42*, 1954. (e) Abdelrazzaq, F. B.; Kwong, R. C.; Thompson, M. E. *J. Am. Chem. Soc.* **2002**, *124*, 4796.

(6) (a) Chhatwal, M.; Kumar, A.; Awasthi, S. K.; Zharnikov, M.; Gupta, R. D. *J. Phys. Chem. C* **2016**, *120*, 2335. (b) Song, C. K.; Luck, K. A.; Zhou, N.; Zeng, L.; Heitzer, H. M.; Manley, E. F.; Goldman, S.; Chen, L. X.; Ratner, M. A.; Bedzyk, M. J.; Chang, R. P. H.; Hersam, M. C.; Marks, T. J. *J. Am. Chem. Soc.* **2014**, *136*, 17762. (c) Schott, M.; Lorrmann, H.; Szczerba, W.; Beck, M.; Kurth, D. G. *Sol. Energy Mater. Sol. Cells* **2014**, *126*, 68. (d) Lindsey, J. S.; Bocian, D. F. *Acc. Chem. Res.* **2011**, *44*, 638. (e) Yao, C.-J.; Zhong, Y.-W.; Nie, H.-J.; Abruña, H. D.; Yao, J. *J. Am. Chem. Soc.* **2011**, *133*, 20720.

(7) (a) Sakamoto, R.; Wu, K.-H.; Matsuoka, R.; Maeda, H.; Nishihara, H. *Chem. Soc. Rev.* **2015**, *44*, 7698. (b) Musumeci, C.; Zappalà, G.; Martsinovich, N.; Orgiu, E.; Schuster, S.; Quici, S.; Zharnikov, M.; Troisi, A.; Licciardello, A.; Samorì, P. *Adv. Mater.* **2014**, *26*, 1688. (c) Ahrenholtz, S. R.; Epley, C. C.; Morris, A. J. *J. Am. Chem. Soc.* **2014**, *136*, 2464. (d) Terada, K.; Nakamura, H.; Kanaizuka, K.; Haga, M.; Asai, Y.; Ishida, T. *ACS Nano* **2012**, *6*, 1988. (e) Tuccitto, N.; Ferri, V.; Cavazzini, M.; Quici, S.; Zhavnerko, G.; Licciardello, A.; Rampi, M. A. *Nat. Mater.* **2009**, *8*, 41.

(8) (a) Nagashima, T.; Ozawa, H.; Suzuki, T.; Nakabayashi, T.; Kanaizuka, K.; Haga, M. *Chem. - Eur. J.* **2016**, *22*, 1658. (b) Balgley, R.; Shankar, S.; Lahav, M.; van der Boom, M. E. *Angew. Chem., Int. Ed.* **2015**, *54*, 12457. (c) de Ruiter, G.; Lahav, M.; van der Boom, M. E. *Acc. Chem. Res.* **2014**, *47*, 3407. (d) de Ruiter, G.; van der Boom, M. E.

Acc. Chem. Res. **2011**, *44*, 563. (e) Altman, M.; Shukla, A. D.; Zubkov, T.; Evmenenko, G.; Dutta, P.; van der Boom, M. E. *J. Am. Chem. Soc.* **2006**, *128*, 7374.
(9) (a) Medishetty, R.; Park, I.-H.; Lee, S. S.; Vittal, J. J. *Chem. Commun.* **2016**, *52*, 3989. (b) Park, I.-H.; Chanthapally, A.; Zhang, Z.; Lee, S. S.; Zaworotko, M. J.; Vittal, J. J. *Angew. Chem., Int. Ed.* **2014**, *53*, 414. (c) MacGillivray, L. R.; Reid, J. L.; Ripmeester, J. A. *J. Am. Chem. Soc.* **2000**, *122*, 7817. (d) McMahon, J. J.; Dougherty, T. P.; Riley, D. J.; Babcock, G. T.; Carter, R. L. *Surf. Sci.* **1985**, *158*, 381. (e) Addadi, L.; van Mil, J.; Lahav, M. *J. Am. Chem. Soc.* **1982**, *104*, 3422.
(10) Lin-Vien, D.; Colthup, N. B.; Fateley, W. G.; Grasselli, J. G. *The Handbook of Infrared and Raman Characteristic Frequencies of Organic Molecules*; Academic Press: Boston, 1991.
(11) (a) Abruna, H. D.; Denisevich, P.; Umana, M.; Meyer, T. J.; Murray, R. W. *J. Am. Chem. Soc.* **1981**, *103*, 1. (b) Denisevich, P.; Willman, K. W.; Murray, R. W. *J. Am. Chem. Soc.* **1981**, *103*, 4727. (c) Murray, R. W. *Molecular Design of Electrode Surfaces*; Wiley: New York, 1992.
(12) Motiei, L.; Kaminker, R.; Sassi, M.; van der Boom, M. E. *J. Am. Chem. Soc.* **2011**, *133*, 14264.
(13) (a) Dickinson, E. J. F.; Limon-Petersen, J. G.; Rees, N. V.; Compton, R. G. *J. Phys. Chem. C* **2009**, *113*, 11157. (b) Nishimori, Y.; Kanaizuka, K.; Murata, M.; Nishihara, H. *Chem. - Asian J.* **2007**, *2*, 367. (c) Saveant, J. M. *J. Phys. Chem.* **1988**, *92*, 4526.
(14) Hayoun Barak, A.; de Ruiter, G.; Lahav, M.; Sharma, S.; Gidron, O.; Evmenenko, G.; Dutta, P.; Bendikov, M.; van der Boom, M. E. *Chem. - Eur. J.* **2013**, *19*, 8821.
(15) Evmenenko, G.; van der Boom, M. E.; Kmetko, J.; Dugan, S. W.; Marks, T. J.; Dutta, P. *J. Chem. Phys.* **2001**, *115*, 6722.
(16) (a) Van Dyck, C.; Ratner, M. A. *Nano Lett.* **2015**, *15*, 1577. (b) MacVittie, K.; Katz, E. *Chem. Commun.* **2014**, *50*, 4816.
(17) (a) Choudhury, J.; Kaminker, R.; Motiei, L.; de Ruiter, G.; Morozov, M.; Lupo, F.; Gulino, A.; van der Boom, M. E. *J. Am. Chem. Soc.* **2010**, *132*, 9295. (b) Motiei, L.; Altman, M.; Gupta, T.; Lupo, F.; Gulino, A.; Evmenenko, G.; Dutta, P.; van der Boom, M. E. *J. Am. Chem. Soc.* **2008**, *130*, 8913. (c) Lin, W.; Lin, W.; Wong, G. K.; Marks, T. J. *J. Am. Chem. Soc.* **1996**, *118*, 8034. (d) Amoroso, A. J.; Thompson, A. M. W. C.; Maher, J. P.; McCleverty, J. A.; Ward, M. D. *Inorg. Chem.* **1995**, *34*, 4828. (e) Anderson, G. K.; Lin, M. *Inorg. Synth.* **1990**, *28*, 60. (f) Parratt, L. G. *Phys. Rev.* **1954**, *95*, 359.
(18) (a) Shankar, S.; Lahav, M.; van der Boom, M. E. *J. Am. Chem. Soc.* **2015**, *137*, 4050. (b) Hsu, C.-Y.; Zhang, J.; Sato, T.; Moriyama, S.; Higuchi, M. *ACS Appl. Mater. Interfaces* **2015**, *7*, 18266. (c) Motiei, L.; Lahav, M.; Freeman, D.; van der Boom, M. E. *J. Am. Chem. Soc.* **2009**, *131*, 3468. (d) Zhang, T.; Liu, S.; Kurth, D. G.; Faul, C. F. J. *Adv. Funct. Mater.* **2009**, *19*, 642.
(19) (a) Frisch, M. J.; Trucks, G. W.; Schlegel, H. B.; Scuseria, G. E.; Robb, M. A.; Cheeseman, J. R.; Scalmani, G.; Barone, V.; Mennucci, B.; Petersson, G. A.; Nakatsuji, H.; Caricato, M.; Li, X.; Hratchian, H. P.; Izmaylov, A. F.; Bloino, J.; Zheng, G.; Sonnenberg, J. L.; Hada, M.; Ehara, M.; Toyota, K.; Fukuda, R.; Hasegawa, J.; Ishida, M.; Nakajima, T.; Honda, Y.; Kitao, O.; Nakai, H.; Vreven, T.; Montgomery, J. A.; Peralta, J. E.; Ogliaro, F.; Bearpark, M.; Heyd, J. J.; Brothers, E.; Kudin, K. N.; Staroverov, V. N.; Keith, T.; Kobayashi, R.; Normand, J.; Raghavachari, K.; Rendell, A.; Burant, J. C.; Iyengar, S. S.; Tomasi, J.; Cossi, M.; Rega, N.; Millam, J. M.; Klene, M.; Knox, J. E.; Cross, J. B.; Bakken, V.; Adamo, C.; Jaramillo, J.; Gomperts, R.; Stratmann, R. E.; Yazyev, O.; Austin, A. J.; Cammi, R.; Pomelli, C.; Ochterski, J. W.; Martin, R. L.; Morokuma, K.; Zakrzewski, V. G.; Voth, G. A.; Salvador, P.; Dannenberg, J. J.; Dapprich, S.; Daniels, A. D.; Farkas, O.; Foresman, J. B.; Ortiz, J. V.; Cioslowski, J.; Fox, D. J. *Gaussian 09*, revision E.01; Gaussian, Inc.: Wallingford, CT, 2013. (b) Perdew, J. P.; Burke, K.; Ernzerhof, M. *Phys. Rev. Lett.* **1996**, *77*, 3865. (c) Perdew, J. P.; Burke, K.; Ernzerhof, M. *Phys. Rev. Lett.* **1997**, *78*, 1396. (d) Schäfer, A.; Horn, H.; Ahlrichs, R. *J. Chem. Phys.* **1992**, *97*, 2571. (e) Weigend, F.; Ahlrichs, R. *Phys. Chem. Chem. Phys.* **2005**, *7*, 3297. (f) Weigend, F. *Phys. Chem. Chem. Phys.* **2006**, *8*, 1057. (g) Dunlap, B. I. *J. Chem. Phys.* **1983**, *78*, 3140. (h) Dunlap, B. I. *J. Mol. Struct.: THEOCHEM* **2000**, *529*, 37.

DOI: 10.1021/jacs.6b09781
J. Am. Chem. Soc. 2016, 138, 16398−16406